Unveiling Frequency-Dependent Electromechanical Dynamics in Ferroelectric BaTiO$_3$ Nanofilm with a Core-Shell Structure

Mingran Zhang [1] , Rui Ma [1], Jianqiang Zhou [1,*], Yuanxiang Zhang [1,*] , Jie Wang [2] and Shengbin Weng [3]

1   Department of Mechanical Engineering, Quzhou University, Quzhou 324000, China;
    zmingran@163.com (M.Z.)
2   College of Aerospace Engineering, Chongqing University, Chongqing 400044, China
3   The Engineering Training Center, Quzhou University, Quzhou 324000, China; weng@qzc.edu.cn
*   Correspondence: zjqaydf@163.com (J.Z.); zhangyx@qzc.edu.cn (Y.Z.)

Abstract: Diverse domain patterns significantly influence the nonlinear electromechanical behaviors of ferroelectric nanomaterials, with polarization switching under strong electric fields being inherently a frequency-dependent phenomenon. Nevertheless, research in this area remains limited. In this study, we present a phase-field investigation of frequency-dependent electromechanical dynamics of a polycrystalline BaTiO$_3$ nanofilm with a core-shell structure, subjected to applied frequencies ranging from 1 to 80 kHz. Our findings elucidate the microstructural mechanisms underlying the electromechanical behaviors observed in these materials. The effect of the grain size and the strains effect are also taken into account. Hysteresis and butterfly loops exhibit a marked change in shape as the frequency changes. We discuss the underlying domain-switching dynamics as a basis for evaluating such frequency-dependent properties. In addition, we examine the scaling behaviors of the dynamic hysteresis and the influence of grain boundaries on the domain structure. We can also observe from hysteresis loops that the remnant polarization and coercive field significantly diminish when grain sizes decrease from 60 to 5 nm. A smaller grain size of the nanofilm yields a larger percentage of the dielectric grain boundary, which "dilutes" the overall ferroelectricity of the film. A vortex domain structure is more likely to form at low frequency and a small grain size.

Keywords: nanoscale ferroelectrics; core-shell structure; frequency dependence; grain size; phase-field method

1. Introduction

Ferroelectric nanofilms have attracted growing attention due to their extensive application potential in nonvolatile ferroelectric memories, actuators, and high-density capacitors [1,2]. In response, ferroelectric thin films have attracted increasing attention [3–5], especially since advances in manufacturing technology have allowed film thicknesses to be reduced to several hundred nanometers. Notably, the investigation of frequency effects in ferroelectric films characterized by nanograins or engineered nanostructures warrants particular attention. Multiple scales, different physical properties of constituent phases, and complex domain structures play an important role in influencing domain configurations within these heterogeneous materials [6–8]. Therefore, it is essential to examine the grain-size dependence of hysteresis properties in nanograined ferroelectric films. Vladimir Bystrov et al. [9] employed molecular dynamics methods to calculate the polarization switching time as a function of the electric field and film thickness in nanosized ferroelectric films. Liu et al. [10] found that reduced thickness, a dense microstructure, and low dielectric tunability collectively enhance the energy storage capacity of relaxor ferroelectric films.

The polarization of ferroelectric films under a strong AC field is characterized by the reorientation of the electric polarization, which involves a dynamic process associated with a domain wall movement and is closely related to the frequency of the applied field [11,12]. Wang et al. [13] investigated the ferroelectric phase of HZO thin-films within a strain and

electric fields, and optimized the relevant parameters to make the O-phase more stable. Bedoya-Hincapié et al. [14] used Monte Carlo simulations to analyze the hysteresis loops of ferroelectric thin films, showing results highly consistent with experimental observations of ferroelectric responses. The polarization reversal in ferroelectric nanofilms is significantly influenced by their microstructural characteristics, including microdefects [15], grain boundaries (GB) [16], low-permittivity surface layers, and size effects [17,18]. Nicolas M. Kawahala et al. [19] extracted the physical parameters associated with both phononic and electronic contributions to terahertz (THz) permittivity using the Drude–Lorentz model.

Ferroelectric barium titanate ($BaTiO_3$) with an intrinsic spontaneous polarization displays multiple remarkable properties, which exhibit strong ferroelectric polarization and a weak coercive field. In recent years, scholars have conducted relevant research on dynamic ferroelectric hysteresis $BaTiO_3$ thin films. The grain boundary, which serves as the interface between neighboring grains, may exhibit distinct properties compared to the grain interior. Zhu et al. [20] discovered the switching behavior of antiferroelectric domain structures in response to an applied electric field, revealing that charge defects can induce local ferroelectric domains, which may suppress saturation polarization and reduce the enclosed area of the hysteresis loop. Wang et al. [21] mainly investigated the phenomenon of mechanically induced polarization switching in $BaTiO_3$ ferroelectric thin films using AFM-based experiments and phase-field simulations, and revealed the effects of an epitaxial misfit strain and thin film on the switching behavior. A transition from low-frequency to high-frequency behavior and analysis of the theoretical model to explain the frequency dependence of the domain motion as the cause of this scaling behavior was observed by Zhang et al. [22]. Andreeva, N. V., et al. [23] concluded that the redistribution of oxygen vacancies is responsible for facilitating electron hopping transport in thin polycrystalline barium titanate.

Microdefects and interfacial effects significantly impact the frequency dependence of critical characteristics in ferroelectric thin films [24,25]. These factors introduce additional complexity in understanding the hysteresis behavior and underlying mechanisms in polycrystalline ferroelectric films. Additionally, grain size influences observed in fine-grained ferroelectrics are attributed to multiple interacting factors. Studies have been conducted to clarify these size-dependent phenomena, identifying several intrinsic and extrinsic size-related factors. To investigate further, we are employing phase-field modeling to analyze frequency-dependent polarization reorientation and size effects in $BaTiO_3$ films subjected to a strong electric field. Concurrently, we are studying the scaling behaviors of dynamic ferroelectric hysteresis in polycrystalline $BaTiO_3$ nanofilms.

2. Theory and Model

The dynamic hysteresis behavior of ferroelectric materials is fundamentally governed by their microstructure. In order to acquire a more profound understanding of the microstructural mechanisms affecting the frequency-dependent behavior of nanograined $BaTiO_3$ films under the influence of strong electric fields, we undertook an extensive numerical investigation. In this study, a phase-field model was implemented, which has been widely utilized in addressing various phase transformation [26–29] and microstructural evolution phenomena [30–34]. This modeling approach defines the total free energy, F, which is given by the volume integral of the energy density, ψ, as

$$F = \int \psi \left(P_i, P_{i,j}, \varepsilon_{ij}, D_i \right) dV \tag{1}$$

where P_i is the electrical polarization vector, $P_{i,j}$ its gradient ($P_{i,j} = \partial P_i / \partial x_j$), ε_{ij} the strain tensor, and D_i the electric displacement vector. The components of the electrical polarization are taken as the order parameters of the system. The variational derivative of the free energy with respect to the polarization is given by

$$\frac{\delta F}{\delta P_i} = \frac{\partial \psi}{\partial P_i} - \frac{\partial}{\partial x_j}\left(\frac{\partial \psi}{\partial P_{i,j}}\right), \tag{2}$$

where $\delta F / \delta P_i$ is the thermodynamic conjugate to $\partial P_i / \partial t$, and its negative serves as the thermodynamic driving force for the evolution of the polarization vector, P_i.

During the system's progression toward equilibrium, there is a consistent decrease in total free energy. The evolution of P_i can be effectively related to this driving force through a linear dependency expressed as follows:

$$\frac{\partial P_i(x,t)}{\partial t} = -L_{ij}\frac{\delta F}{\delta P_j(x,t)} \ or \ \beta_{ij}\frac{\partial P_j}{\partial t} = \left(\frac{\partial \psi}{\partial P_{i,j}}\right)_{,j} - \frac{\partial \psi}{\partial P_i} \tag{3}$$

The temporal evolution of the electrical polarization $P_i(i = 1, 2, 3)$ of any position within the nanofilm is described by the time-dependent Ginzburg–Landau (TDGL) equation. where L_{ij} denotes the components of the positive-definite kinetic coefficient matrix, while β_{ij} represents the elements of the inverse mobility tensor. Furthermore, Su and Landis [35] have outlined a general formulation for the free energy density, ψ, within a three-dimensional spatial structure:

$$\begin{aligned}
\psi\left(P_i, P_{i,j}, \varepsilon_{ij}, D_i\right) &= \tfrac{1}{2}a_{ijkl}P_iP_j \\
&+\left\{\tfrac{1}{2}\bar{a}_{ij}P_iP_j + \tfrac{1}{2}\bar{\bar{a}}_{ijkl}P_iP_jP_kP_l + \tfrac{1}{6}\bar{\bar{\bar{a}}}_{ijklnm}P_iP_jP_kP_lP_mP_n\right. \\
&\left.+\tfrac{1}{8}\bar{\bar{\bar{\bar{a}}}}_{ijklnmrs}P_iP_jP_kP_lP_mP_nP_rP_s\right\} \\
&+\left\{b_{ijlk}\varepsilon_{ij}P_kP_l + \tfrac{1}{2}c^H_{ijkl}\varepsilon_{ij}\varepsilon_{kl} + f_{ijklmn}\varepsilon_{ij}\varepsilon_{kl}P_mP_n\right. \\
&\left.+g_{ijklmn}\varepsilon_{ij}P_kP_lP_mP_n\right\} + \tfrac{1}{2\kappa_0}(D_i - P_i)(D_i - P_i).
\end{aligned} \tag{4}$$

The total free energy of this system is fundamentally structured into four components: the initial term accounts for the ferroelectric gradient energy, which is influenced by the spatial polarization changes. The next four terms, within the first set of brackets, describe the Landau free energy, encapsulating the intrinsic polarization characteristics. The four terms following the second set of brackets represent the elastic energy, which contributes to the mechanical stability of the system. The final term corresponds to the energy stored in free space, κ_0 the free space permittivity. In solving this problem, we incorporated a quasi-static Maxwell equation, a mechanical equilibrium equation, and a time-dependent Ginzburg–Landau (TDGL) equation to formulate a weak form of the virtual work principle. This formulation was then applied to conduct numerical solutions via the finite element method. For an extended explanation of this approach, along with details regarding the selection of material parameters, please refer to the relevant literature [30,32,35].

Extensive research has demonstrated that the hysteresis behavior of ferroelectric materials is intricately linked to their microstructural characteristics [36]. Various factors such as lattice structures, crystalline textures, grain sizes, and morphologies, as well as unique properties at the local grain boundaries (GBs), can significantly influence the mobility of ferroelectric domains, thereby impacting the overall hysteresis observed in these materials. The grains within ferroelectrics are oriented in different lattice directions, each showcasing specific behaviors at the interfaces between adjacent grains and within the grains themselves. In the core-shell model illustrated in Figure 1, the grain boundary is represented by the gray zone, while the interior of the nanograins is depicted in a multi-colored zone. The thin film unit serves as a representative segment of the entire nanofilm material, characterized by numerous randomly oriented grains. Periodic boundary conditions are applied to both ends of the thin film unit. The grain boundary is conceptualized as a "dead layer" where the polarization is entirely suppressed. The dielectric permittivity of this grain boundary is assumed to be 35% of the inside of the grain. Furthermore, the thickness of the GB is estimated to be between two and three atomic spacings (approximately 0.8 nm)

and remains constant regardless of the grain size [37]. Notably, smaller grain sizes tend to exhibit a more complex domain structure and pronounced electromechanical behaviors in ferroelectric polycrystalline materials due to the influence of grain boundaries [38]. We hence set the average grain size to 15 nm. As shown in Figure 1, the local crystal-lattice orientations φ vary gradually from $0°$ to $90°$ between the global coordinates x_i^G and the local coordinates $x_i^L (i = 1,2)$.
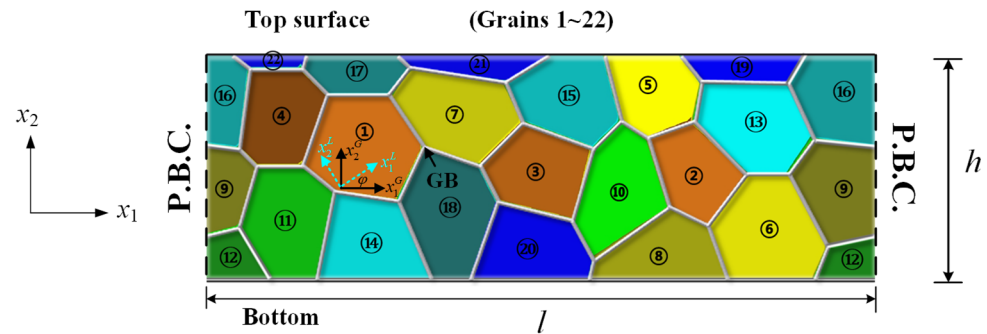

Figure 1. Schematic of a the BaTiO$_3$ polycrystalline nano film with 22 grains (core-shell) and marked orientation of each grain mentioned.

In this work, the nanofilm system is modeled as a two-dimensional (2D) problem. All computational analyses are conducted based on the assumption of a planar configuration, which implies that the z-components are effectively neglected (i.e., $P_z = 0$, $E_z = 0$, $D_z = 0$ and $\sigma_{xz} = \sigma_{yz} = 0$). To accurately represent the characteristics of the nanofilm structure, a film segment is constructed with suitable boundary conditions. To investigate the ferroelectric hysteresis loops, an external vertical electric field is applied to the thin film, described by the equation:

$$E = E_{max}\sin(2\pi f \cdot t), \tag{5}$$

where E_{max} denotes the amplitude of the electric field, t represents the time variable, and f is the loading frequency. We consider the top surface of the film to be unconstrained, while both the displacement and electric potential are maintained at zero along the bottom boundary. The applied electric field must be sufficiently high to ensure complete polarization switching; thus, we selected $E_{max} = 8E_0$, with E_0 defined as 218 kV/cm [3,30,35].

The influences of the grain boundaries and film-substrate misfit strain are taken into account. The strain components are defined as $\varepsilon_{xz} = \varepsilon_{yz} = 0$ and $\varepsilon_{zz} = \bar{\varepsilon}$, where $\bar{\varepsilon}$ represents the in-plane strain arising from the lattice mismatch between the nanofilm and the substrate [39]. This in-plane strain is treated as a uniform application across the film, exerted on both sides via mechanical displacement boundary conditions: $u_x(0, y) = u_x(l, y) + l\bar{\varepsilon}$, $u_y(0, y) = u_y(l, y)$ (the length of the representative film segment is set as l). For the left and right sides of the nanofilm, the periodic boundary conditions of electric potential and polarization are also given as $\phi(0, y) = \phi(l, y)$, $P_x(0, y) = P_x(l, y)$ and $P_y(0, y) = P_y(l, y)$, respectively. All material constants utilized in this phase-field simulation are sourced from the work of Su and Landis [35].

3. Results and Discussion

3.1. The Frequency-Dependent and Size Effect of Dynamic Hysteresis

The computation under each preselected frequency is run with sufficient time steps to make sure that a stable response can be observed. The reference values for the electric displacement, the electric field, and the strain constant are established at $P_0 = 0.26$ C/m^2, $E_0 = 218$ kV/cm and $\varepsilon_0 = 0.82\%$, respectively, with the in-plane strain set as -0.1%. The resulting hysteresis and butterfly loops for each selected frequency are depicted in Figure 2a,b, respectively. It is clear that, at relatively low frequencies, the hysteresis and butterfly loops maintain conventional shapes. However, when the frequency reaches 20 kHz, noticeable changes in both loops begin to occur. Specifically, the hysteresis loop

transforms into an elliptical shape starting at 20 kHz, while the butterfly loop evolves into a kidney shape at 40 kHz, subsequently becoming elliptical at 80 kHz. As the frequency increases, the sharp tails of the butterfly loops gradually fade away. Clearly, the frequency-dependent behaviors of polycrystalline BaTiO$_3$ nanofilms can be categorized into two distinct frequency phases: a low frequency from 1 to 20 kHz, and a high frequency from 20 to 80 kHz. Previous studies have documented similar unconventional shapes of hysteresis and butterfly loops at elevated frequencies. Liu et al. [40] experimentally observed that the hysteresis loop shape transitions from a slender rhombic form to an elliptical configuration as the frequency varies from 10^{-5} to 10^2 kHz. Moreover, Richman et al. [41] employed the second-order Landau model to numerically simulate the dynamic hysteresis response of ferroelectric systems, revealing that the hysteresis loop also adopts an elliptical shape at a high frequency.
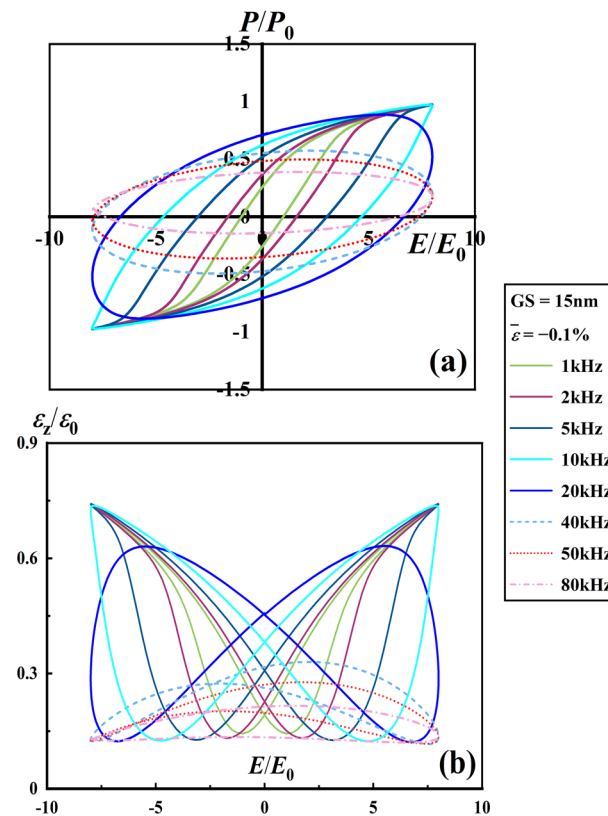

Figure 2. The calculated (**a**) hysteresis loops and (**b**) butterfly loops at different frequencies of the BaTiO$_3$ nano-film under an in-plane strain of −0.1%.

In addition, to investigate the effect of the in-plane strain on the frequency dependence of ferroelectric nanofilms, we also calculated the hysteresis loops and the butterfly loops under an epitaxial strain of −2.23%, as shown in Figure 3a,b. Notably, the center of the hysteresis loop exhibits a concave shape at 1 kHz, and both the remnant polarization and coercive field experience a sudden decrease. Once the frequency is increased to 5 kHz, such a concave shape gradually disappears and returns to an elliptical shape. When the grain size is 15 nm, due to the dominant role of dielectric grain boundaries, the film exhibits a significant "two-stage hysteresis" phenomenon under a larger compressive strain (−2.23%). Therefore, at lower frequencies, the in-plane strain has a more significant impact on the ferroelectric properties of thin films. However, as a result of the accelerated polarization reversal at higher frequencies, the ferroelectric response is suppressed, leading to the gradual disappearance of the concave shape of the hysteresis loops.
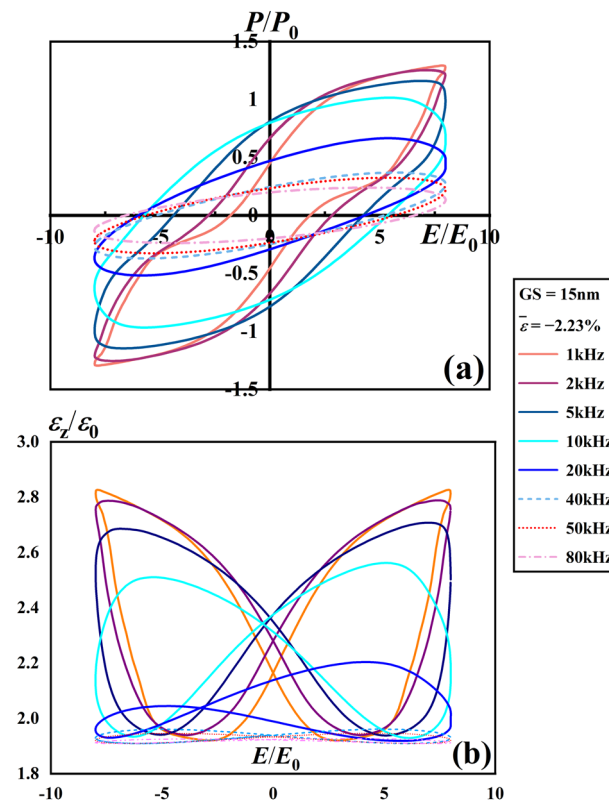
Figure 3. The calculated (**a**) hysteresis loops and (**b**) butterfly loops at different frequencies of the BaTiO$_3$ nano-film under an in-plane strain of -2.23%.

The frequency-related parameters at the remnant state were measured under two epitaxial strains, specifically -0.1% and -2.23%. The results are summarized in Figure 4. The remnant polarization shows an initial increase (as the frequency is raised from 1 to 20 kHz), then drops sharply all the way as the frequency increases to 80 kHz for the in-plane strain of -0.1%. However, the remnant polarization reached its peak at 5 kHz under the epitaxial strain of -2.23%, as plotted in red dotted lines. As the frequency increases, the remnant polarization decreases more sharply than when the strain is -0.1%. The coercive field exhibited an increase until 20 kHz; but it decreased slowly afterwards for the in-plane strain of -0.1%. When the in-plane strain is -2.23%, the coercive field initially exhibits a sharp increase, followed by a slight decrease, and subsequently a gradual increase. Both dielectric constants and piezoelectric constants monotonically decrease with frequency under two epitaxial strains. This indicates that the effect of the in-plane strain on the dielectric constants and piezoelectric constants is not significant. Such a first rise and then drop trend of the remnant polarization and the coercive field with the frequency agrees with the earlier experimental observations [40,42,43]; the same calculations were also obtained theoretically [3,11].

For a quantitative analysis of dynamic hysteresis, we examined the scaling behaviors of BaTiO$_3$ polycrystalline nanofilms. The results, along with the fitting curves, are presented in Figure 5 for the low and high frequency, respectively. The scaling law, represented by the hysteresis area $\langle A \rangle$ as a function of frequency f and field amplitude E_0, is a critical factor in evaluating the key kinetics associated with domain nucleation, growth, and motion. It has been found that the scaling relation between E_0 and f follows the power law in most systems as: $\langle A \rangle \propto f^{\alpha} E_0^{\beta}$, where the exponents α and β are contingent upon the dimensionality and symmetry of the system [44,45]. In this work, we maintain the amplitude of the electric field at a constant value, thereby allowing for the consideration of the scaling law solely in relation to the frequency, which can be denoted as $\langle A \rangle \propto f^{\alpha}$, where the exponent α is the slope of $\log_{10} A$ and $\log_{10} f$. The fitted exponent α is 0.42 in

the low-frequency range, while the fitted exponent α is -0.97 in the high-frequency range, as shown in Figure 5. Studies indicate that this frequency-dependent scaling exponent is consistent with the experimental and theoretical results of dynamic scaling behavior in ferroelectric thin film systems observed earlier [44,46].
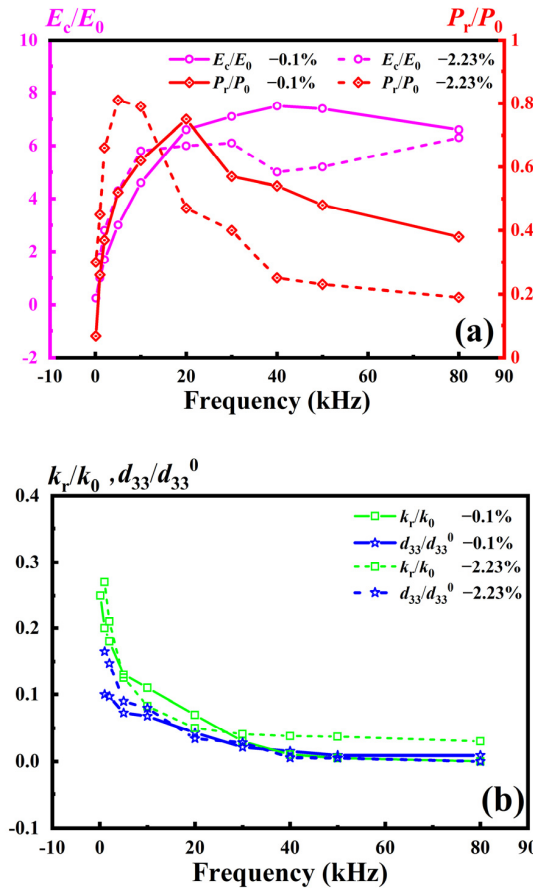

Figure 4. The frequency-related parameters of (**a**) the coercive field and remnant polarization; (**b**) the piezoelectric coefficient and dielectric constant. ($\kappa_0 = P_0/E_0$, $d_{33}^0 = \varepsilon_0/E_0$).
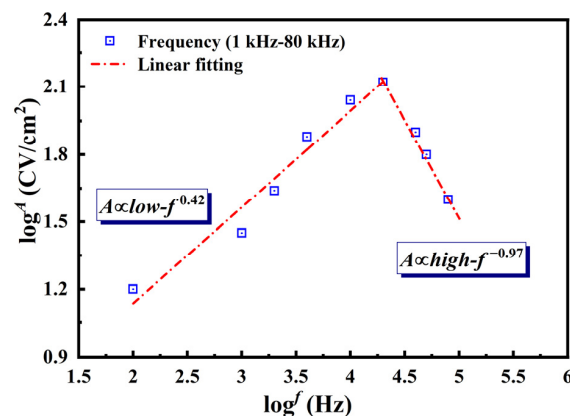

Figure 5. Scaling plots of loop area A against f for BaTiO$_3$ polycrystalline nanofilm at low frequency and high frequency.

Liu et al. [46,47] experimentally studied the hysteresis scaling behavior of ferroelectric thin films within the frequency range of 10^{-2} to 10^{5} Hz. They found that the scaling exponent in the low-frequency range is 1/3, while in the high-frequency range, it became $-2/3$. Similarly, Guo et al. [44] experimentally measured the intrinsic scaling of PBZT

ferroelectric thin films; the frequency-dependent scaling relation followed $\langle A \rangle \propto f^{0.35}$, but at higher frequencies, the power-law exponent was -0.32. The findings from both experimental and theoretical investigations indicate that, within the low-frequency range, the theoretical results exhibit a general consistency with the experimental data. Conversely, in the high-frequency range, there is a notable variation in the frequency-dependent scaling exponent. This discrepancy can be attributed primarily to the hysteresis behavior observed at low frequencies, which is largely a consequence of intrinsic domain switching within the thin film. As the loading frequency increases, the depolarization field exerts a significant suppressive effect on the polarization, resulting in a more pronounced divergence between theoretical predictions and experimental observations in the high-frequency range.

3.2. Grain Size Effect of BaTiO₃ Nano-Polycrystalline Film

The calculated hysteresis loops and butterfly loops under the average grain size being 60 nm, 30 nm, 15 nm, 10 nm, and 5 nm, respectively, are plotted in Figure 6. For each computation, a constant frequency was set as 1 kHz under the strong electric field, wherein the value of the in-plane strain was set at -0.1%. The hysteresis loop, as illustrated in Figure 6a, exhibits conventional shapes within grain-size ranges from 60 to 10 nm; then the loops become severely tilted at 5 nm and the behavior approaches a super-paraelectric characteristic. The butterfly loops related to the nonlinear electromechanical coupling behavior, as shown in Figure 6b. The butterfly shapes to an arc shape, and the "wings" of the butterfly loop vanish when the grain size is set to 5 nm. This phenomenon confirms that polarization switching in the ferroelectric material is frozen once the grain size is below 5 nm. As the grain size of the thin film increases, the relative proportion of the grain boundaries diminishes, consequently leading to a gradual reduction in their influence on the ferroelectric properties of the thin film. The series of results revealed that the grain boundary plays a significant role in a small grain size.
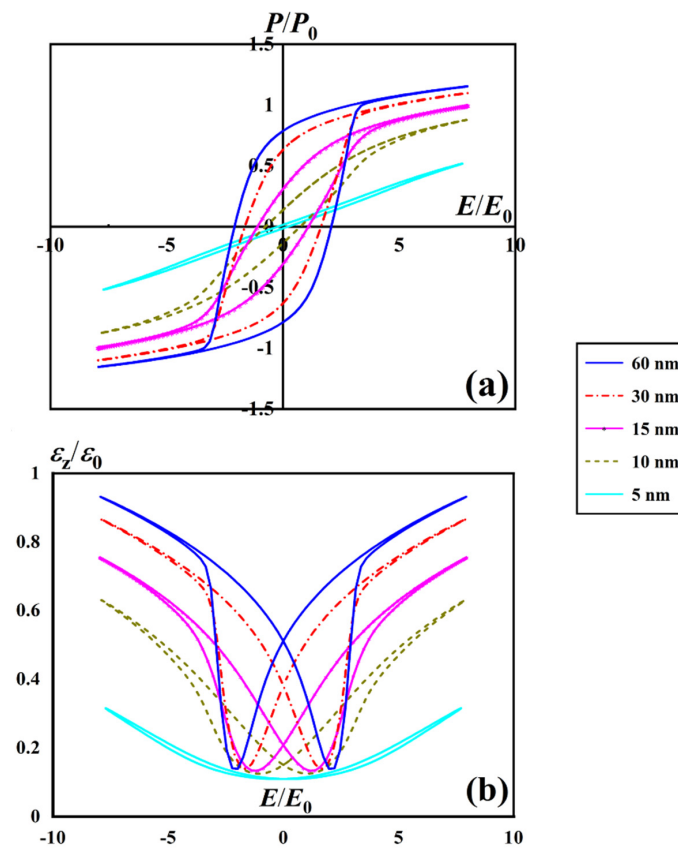

Figure 6. (**a**) The hysteresis loops and (**b**) the butterfly loops with different grain sizes of polycrystalline nanofilms.

The entire variations in the coercive field E_c, dielectric permittivity κ_r and piezoelectric coefficient d_{33} were plotted in Figure 7 as the average grain size decreased from 60 to 5 nm. The coercive field and piezoelectric coefficient decrease as the grain size decreases, as shown in Figure 7a. However, the dielectric permittivity first displayed a sharp increase and then an abrupt drop, and the peak value was reached at 15 nm. The simulated remnant polarization P_r compared with experimental observations is summarized in Figure 7b. The remnant polarization shows a monotonically decreasing trend as the grain size gradually decreases, which is consistent with the observed experiment in the trend for the corresponding grain sizes in [42,48–51]. Variations in specific values may arise from differences in selected material parameters and the actual compositions of the tested samples, as the dynamics of polarization switching are highly sensitive to these parameters.
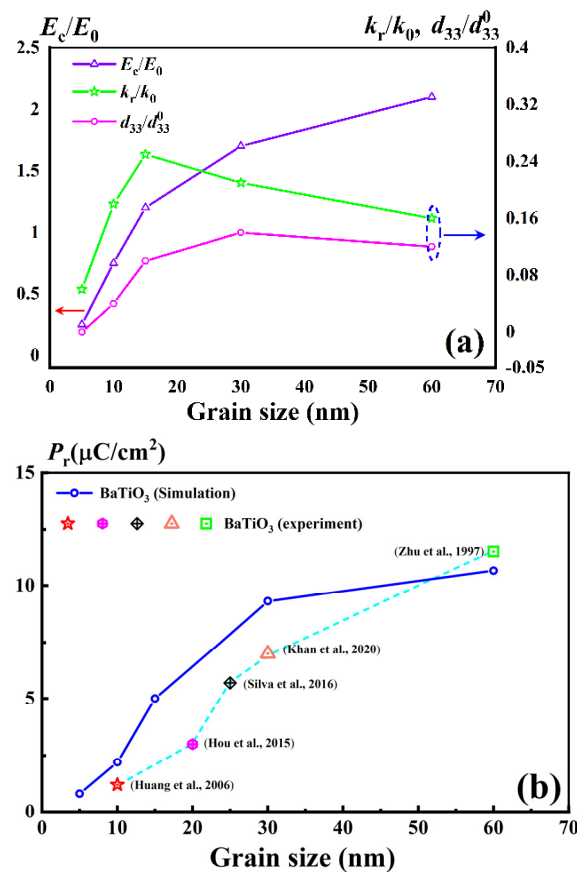

Figure 7. The calculated properties against the grain size: (**a**) the coercive field, the dielectric permittivity, and piezoelectric coefficient at the zero electric field; (**b**) the remnant polarization and other experimental data ($\kappa_0 = P_0/E_0$, $d_{33}^0 = \varepsilon_0/E_0$) [42,48–51].

Furthermore, the dielectric permittivity of BaTiO$_3$ nanofilms with grain sizes below 15 nm appears particularly responsive to the presence of a low-permittivity, non-ferroelectric grain boundary layer. A smaller grain size of the nanofilm yields a larger percentage of dielectric grain boundary, which "dilutes" the overall ferroelectricity of the film. A smaller value of the parameter related to the ferroelectric properties under a smaller grain size was caused by the intrinsic-dominated. Instead, the intrinsic effect is negligible at larger grain sizes; it is the external effects such as the distribution of the domain structure and the motility of the domain walls that result in a lower dielectric permittivity.

3.3. Underlying Domain Dynamics

To enhance our understanding of the origin mechanism behind the frequency dependence, we examined the domain structures at selected frequencies of 0.1 kHz (low

frequency) and 50 kHz (high frequency) under various electric field loading conditions, as shown in Figures 8 and 9.
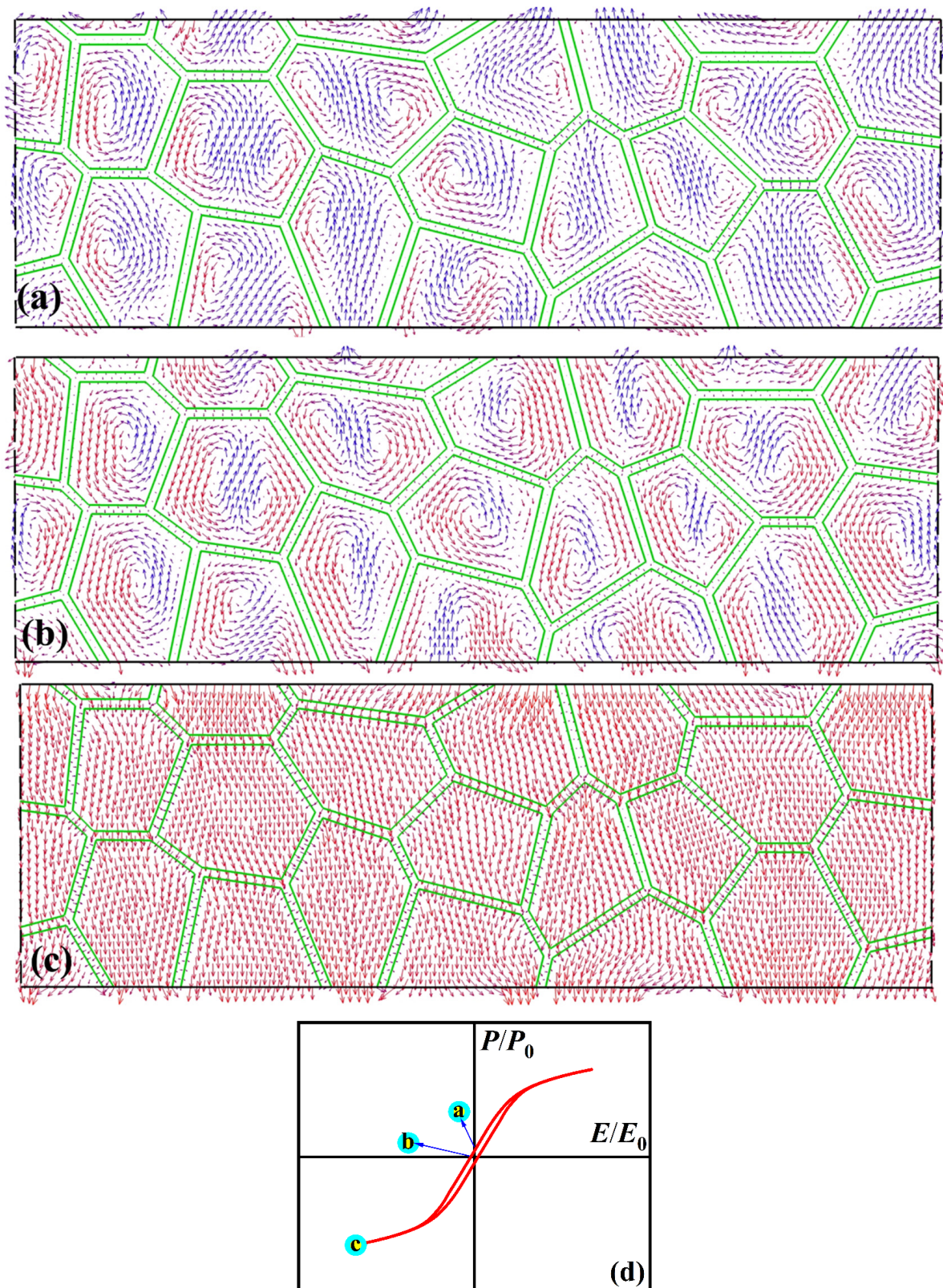

Figure 8. The microstructure of the BaTiO$_3$ nanofilm at frequency 0.1 kHz (**a**) $E = 0$; (**b**) $E = -0.25E_0$; (**c**) $E = -8E_0$; (**d**) the corresponding positions of different states in the hysteresis loop.

Figure 9. The microstructure of the BaTiO$_3$ nanofilm at frequency 50 kHz (**a**) $E = 0$; (**b**) $E = -7.8E_0$; (**c**) $E = 0$; (**d**) the corresponding positions of different states in the hysteresis loop.
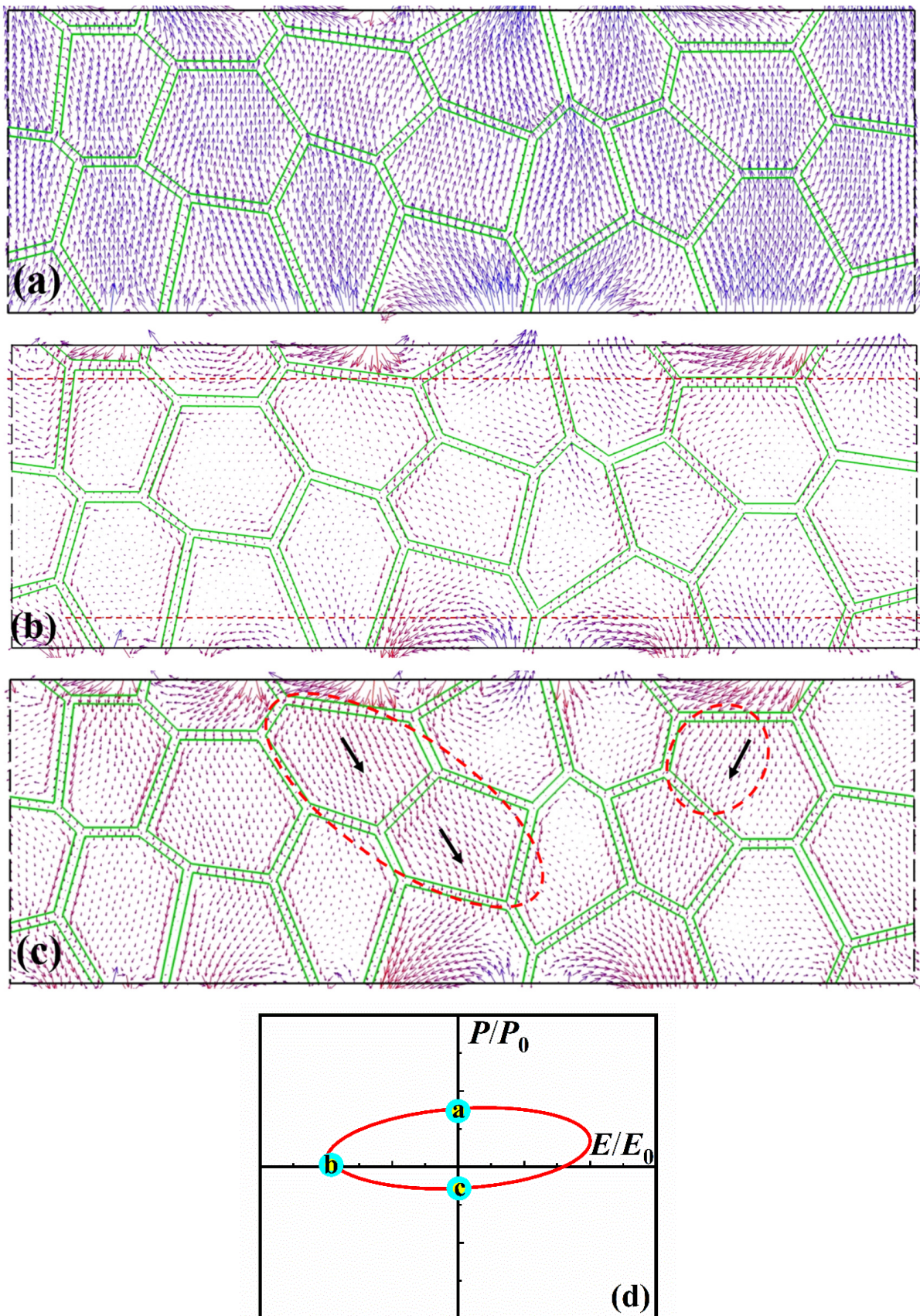
In the remnant state, some grains display vortex domain structures, as illustrated in Figure 8a. Figure 8b shows that the number of these vortex domain structures gradually increases, appearing in nearly all grains. As the electric field rises to its maximum value, these vortex domain structures gradually diminish. At the same time, the polarization vectors point upward, resulting in a single domain structure, as depicted in Figure 8c. The polarization distribution near the grain boundaries is non-uniform, leading to the generation of a strong depolarization field, which inhibits polarization switching and induces the formation of vortex domain structures. However, these vortex structures are more readily reversible compared to mono-domain structures, which contribute to a reduced remnant polarization and coercive field.

As the frequency increases, the polarization switching speed begins to lag, resulting in a significant decrease in the remnant polarization. The polarization distribution of the nanofilm at an electric field frequency of 80 kHz is depicted in Figure 9a–c. It is evident that the polarization cannot achieve a 180° reversal. This is because the electric field loading speed is too fast. In Figure 9c, the polarization is limited to a 90° switching (indicated by the red oval dashed line) during each cycle of the electric field loading. The microstructural interactions within the individual nanograins are intensified at high frequencies, which suppress polarization switching and lead to a larger coercive field. Furthermore, high-frequency loading does not allow sufficient time for the polarization vectors to switch, resulting in a gradual decrease in the dielectric and piezoelectric constants as the applied frequency increases.

The reorientation of polarization leads to microstructural changes, which are fundamental to the macroscopic nonlinear electromechanical behavior observed in ferroelectric materials. To investigate the mechanism behind domain structure formation induced by a strong AC field across various grain sizes, a constant frequency of 1 kHz was employed in conjunction with a strong electric field of $8E_0$. The polarization distributions at the remnant state with the average grain size being 10, 15, and 30 nm, are displayed in Figure 10. The polarization vectors are all upward and exhibit a single domain structure with the larger grain size, as shown in Figure 10c. The vortex domain pattern gradually disappears. The presence of the grain boundary makes it easier for vortex domain structures to appear. From the domain structure, it can be seen that vortex domain structures are present at lower frequencies and smaller grain sizes. This finding offers valuable theoretical insights for optimizing and advancing the ferroelectric thin film memory.

To further reveal the mechanism of domain structure induced by in-plane strains. The distribution of the polycrystalline nanofilm at frequency 5 kHz under in-plane strains −2.23% is displayed in Figure 11. In the remnant-state polarization state, most grains exhibit vertically upward single domain structures, while some grains exhibit 90° domains, as shown in Figure 11a. As the electric field is reverse-loaded to the coercive field state, a complex multi-domain structure (180° domains and vortex domains) appears inside the grain. An excessive compressive strain intensifies the internal interaction forces between the grains and grain boundaries, thus leading to the formation of a complex domain structure. Meanwhile, under a different in-plane strain, the dynamic microstructure of ferroelectric thin films can exhibit diversity while the role of the grain boundaries is also crucial. Therefore, selecting appropriate substrates and electrical parameters can further control the electrical properties of ferroelectric polycrystalline materials by regulating the distribution of micro-domain structures.
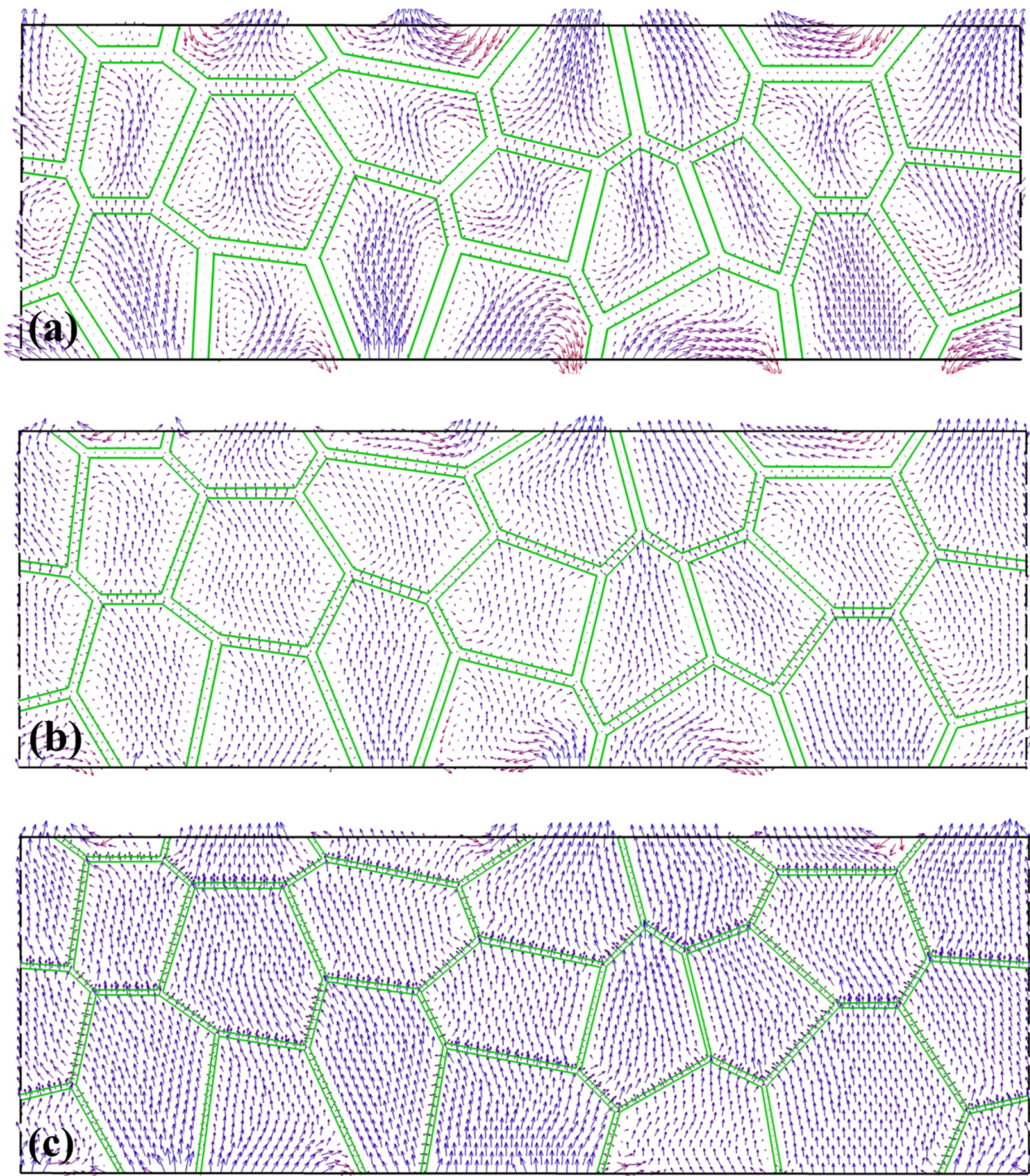
Figure 10. The remnant-state polarization distribution of the polycrystalline nanofilm with the grain sizes being (**a**) 10 nm; (**b**) 15 nm; (**c**) 30 nm.
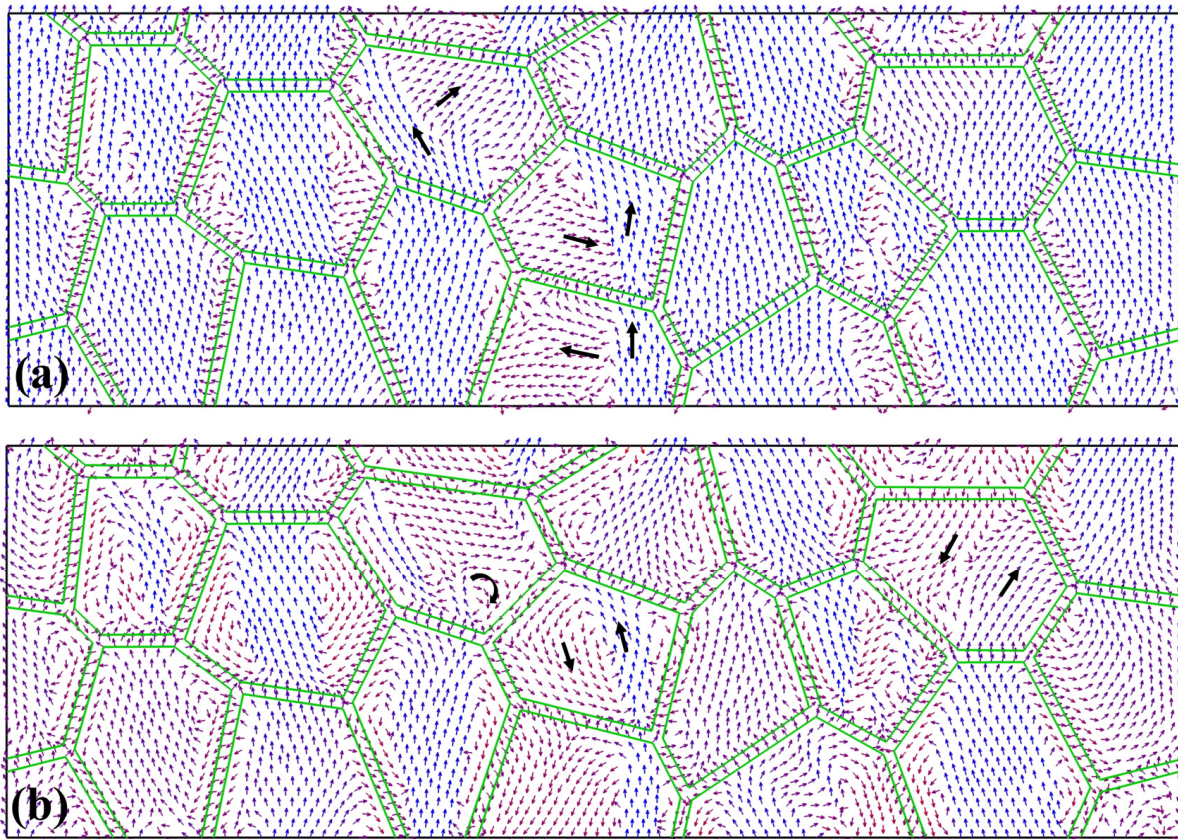
Figure 11. The microstructure of the nanofilm at frequency 5 kHz under in-plane strains −2.23%:
(**a**) the remnant-state polarization; (**b**) the coercive field state.

4. Conclusions

In summary, we numerically investigated the influence of grain boundaries and the in-plain strain of frequency-driven polarization switching of a BaTiO$_3$ nanofilm with a core-shell structure. The calculations were performed on a polycrystalline nanofilm with a grain size of 15 nm, and the preselected frequency range varied from 1 to 80 kHz under the in-plane strains −0.1% and −2.23%. Analysis of the hysteresis and butterfly loops within −0.1% revealed that conventional hysteresis behavior is observed at frequencies of 10 kHz and below. As the applied frequency exceeds 20 kHz, the hysteresis loop transitions to an elliptical and kidney-shaped configuration, respectively. It has been demonstrated that larger compressive strains (−2.23%) lead to a significant "two-stage hysteresis" phenomenon at 1 kHz. The dielectric constant and piezoelectric coefficient are very little affected by the in-plane strain, but the residual polarization and corrected field are affected significantly. The polarization has enough time to achieve 180° full reversal within a low-frequency range; however, at higher frequencies, only 90° switching occurs in certain grains. It was also observed that vortex domains are more likely to form at lower applied frequencies or with smaller grain sizes. Ferroelectric properties of thin films are more affected by an in-plane strain at lower frequencies. Additionally, the polar vortex domain structure has significant implications for ultra-high density and ultra-fast information storage devices as well as modulating physical properties.

Author Contributions: Conceptualization, M.Z. and Y.Z.; methodology, M.Z.; software, R.M.; validation, M.Z., R.M. and J.W.; formal analysis, Y.Z.; investigation, M.Z.; resources, J.W.; data curation, J.W.; writing—original draft preparation, M.Z.; writing—review and editing, M.Z.; supervision, S.W.; project administration, J.Z.; funding acquisition, J.Z. All authors have read and agreed to the published version of the manuscript.

Institutional Review Board Statement: Not applicable.

Informed Consent Statement: Not applicable.

Data Availability Statement: The data are contained within the article.

Conflicts of Interest: The authors declare no conflicts of interest.

References

1. Pan, H.; Ma, J.; Ma, J.; Zhang, Q.; Liu, X.; Guan, B.; Gu, L.; Zhang, X.; Zhang, Y.J.; Li, L.; et al. Giant energy density and high efficiency achieved in bismuth ferrite-based film capacitors via domain engineering. *Nat. Commun.* **2018**, *9*, 1813. [CrossRef] [PubMed]
2. Das, A.K.; Raul, C.K.; Karmakar, R.; Meikap, A.K. Study of enhanced dielectric permittivity of functionalize multiwall carbon nanotube-based polyvinylidene fluoride free-standing film for flexible storage device. *Phys. Lett. A* **2021**, *407*, 127455. [CrossRef]
3. Zhang, Q.N.; Xia, X.D.; Wang, J.; Su, Y. Effects of epitaxial strain, film thickness and electric-field frequency on the ferroelectric behavior of $BaTiO_3$ nano films. *Int. J. Solids Struct.* **2018**, *144–145*, 32–45. [CrossRef]
4. Nahas, Y.; Prokhorenko, S.; Fischer, J.; Xu, B.; Carretero, C.; Prosandeev, S.; Bibes, M.; Fusil, S.; Dkhil, B.; Garcia, V.; et al. Inverse transition of labyrinthine domain patterns in ferroelectric thin films. *Nature* **2020**, *577*, 47–51. [CrossRef]
5. Shan, D.L.; Lei, C.H.; Cai, Y.C.; Pan, K.; Liu, Y.Y. Mechanical control of electrocaloric response in epitaxial ferroelectric thin films. *Int. J. Solids Struct.* **2021**, *216*, 59–67. [CrossRef]
6. Tang, Y.L.; Zhu, Y.L.; Ma, X.L.; Borisevich, A.Y.; Morozovska, A.N.; Eliseev, E.A.; Wang, W.Y.; Wang, Y.J.; Xu, Y.B.; Zhang, Z.D.; et al. Observation of a periodic array of flux-closure quadrants in strained ferroelectric $PbTiO_3$ films. *Science* **2015**, *348*, 547–551. [CrossRef]
7. Yadav, A.K.; Nelson, C.T.; Hsu, S.L.; Hong, Z.; Clarkson, J.D.; Schleputz, C.M.; Damodaran, A.R.; Shafer, P.; Arenholz, E.; Dedon, L.R.; et al. Observation of polar vortices in oxide superlattices. *Nature* **2016**, *530*, 198–201. [CrossRef]
8. Van Winkle, M.; Dowlatshahi, N.; Khaloo, N.; Iyer, M.; Craig, I.M.; Dhall, R.; Taniguchi, T.; Watanabe, K.; Bediako, D.K. Engineering interfacial polarization switching in van der Waals multilayers. *Nat. Nanotechnol.* **2024**, *19*, 751–757. [CrossRef]
9. Bystrov, V.; Paramonova, E.; Meng, X.; Shen, H.; Wang, J.; Lin, T.; Fridkin, V. Ferroelectric thin films and composites based on polyvinylidene fluoride and graphene layers: Molecular dynamics study. *Coatings* **2024**, *14*, 356. [CrossRef]
10. Liu, X.; Yao, Y.; Wang, X.; Zhao, L.; San, X. Energy Storage Performance of $(Na_{0.5}Bi_{0.5})TiO_3$ Relaxor Ferroelectric Film. *Coatings* **2024**, *14*, 801. [CrossRef]
11. Zhang, Q.N.; Su, Y. The frequency dependence of electromechanical behaviors of columnar-grained $BaTiO_3$ nanofilms. *Phys. Lett. A* **2020**, *384*, 126374. [CrossRef]
12. Lente, M.H.; Picinin, A.; Rino, J.P.; Eiras, J.A. 90° domain wall relaxation and frequency dependence of the coercive field in the ferroelectric switching process. *J. Appl. Phys.* **2004**, *95*, 2646–2653. [CrossRef]
13. Wang, L.; Wang, C.; Zhou, L.; Zhou, X.; Pan, Y.; Wu, X.; Ji, W. Optimal parameter-space for stabilizing the ferroelectric phase of $Hf_{0.5}Zr_{0.5}O_2$ thin-films under strain and electric fields. *Chin. Phys. B* **2024**, *33*, 076803. [CrossRef]
14. Bedoya-Hincapié, C.M.; Ortiz-Álvarez, H.H.; Restrepo-Parra, E.; Olaya-Flórez, J.J.; Alfonso, J.E. Hysteresis loop behaviors of ferroelectric thin films: A Monte Carlo simulation study. *Chin. Phys. B* **2015**, *24*, 117701. [CrossRef]
15. Kumar, M.; Shankar, S.; Brijmohan Kumar, S.; Thakur, O.P.; Ghosh, A.K. Impedance spectroscopy and conductivity analysis of multiferroic BFO–BT solid solutions. *Phys. Lett. A* **2017**, *381*, 379–386. [CrossRef]
16. Yan, X.; Li, Y.; Zhao, J.; Li, Y.; Bai, G.; Zhu, S. Roles of grain boundary and oxygen vacancies in $Ba_{0.6}Sr_{0.4}TiO_3$ films for resistive switching device application. *Appl. Phys. Lett.* **2016**, *108*, 033108. [CrossRef]
17. Park, S.H.; Kim, J.Y.; Song, J.Y.; Jang, H.W. Overcoming size effects in ferroelectric thin films. *Adv. Phys. Res.* **2023**, *2*, 2200096. [CrossRef]
18. Gao, P.; Zhang, Z.; Li, M.; Ishikawa, R.; Feng, B.; Liu, H.-J.; Huang, Y.-L.; Shibata, N.; Ma, X.; Chen, S.; et al. Possible absence of critical thickness and size effect in ultrathin perovskite ferroelectric films. *Nat. Commun.* **2017**, *8*, 15549. [CrossRef]
19. Kawahala, N.M.; Matos, D.A.; Rappl PH, O.; Abramof, E.; Baydin, A.; Kono, J.; Hernandez, F.G.G. Thickness-dependent terahertz permittivity of epitaxially grown PbTe thin films. *Coatings* **2023**, *13*, 1855. [CrossRef]
20. Zhu, J.; Liu, Z.; Zhong, B.; Wang, Y.; Xu, B. Domain size and charge defects affecting the polarization switching of antiferroelectric domains. *Chin. Phys. B* **2023**, *32*, 047701. [CrossRef]
21. Wang, B.; Lu, H.; Bark, C.W.; Eom, C.B.; Gruverman, A.; Chen, L.Q. Mechanically induced ferroelectric switching in $BaTiO_3$ thin films. *Acta Mater.* **2020**, *193*, 151–162. [CrossRef]
22. Zhang, M.; Deng, C. Scaling behavior of dynamic hysteresis in epitaxial ferroelectric $BaTiO_3$ thin films. *J. Alloys Compd.* **2021**, *883*, 160864. [CrossRef]
23. Andreeva, N.V.; Ryndin, E.A.; Petukhov, A.E.; Vilkov, O.Y.; Al-Saman, A.A. Dynamics of analog switching behavior in thin polycrystalline Barium Titanate. *Adv. Electron. Mater.* **2024**, *10*, 2300806. [CrossRef]

24. Mai, M.; Zhu, C.; Liu, G.; Ma, X. Effect of dielectric layer on ferroelectric responses of P(VDF-TrFE) thin films. *Phys. Lett. A* **2018**, *382*, 2372–2375. [CrossRef]

25. Pečnik, T.; Glinšek, S.; Kmet, B.; Malič, B. Combined effects of thickness, grain size and residual stress on the dielectric properties of $Ba_{0.5}Sr_{0.5}TiO_3$ thin films. *J. Alloys Compd.* **2015**, *646*, 766–772. [CrossRef]

26. Wang, F.; Liu, T.; Xie, C.L.; Liu, Y.; Ma, N.S.; Duan, J.; He, J.R.; Li, B.; Ou, B.L.; Ou, Y.; et al. Temperature-electric field hysteresis loop of multicaloric effects in $PbZr_{0.8}Ti_{0.2}O_3$ thin films. *Phys. Lett. A* **2019**, *383*, 2933–2937. [CrossRef]

27. Van Lich, L.; Shimada, T.; Sepideh, S.; Wang, J.; Kitamura, T. Multilevel hysteresis loop engineered with ferroelectric nano-metamaterials. *Acta Mater.* **2017**, *125*, 202–209. [CrossRef]

28. Renuka Balakrishna, A.; Huber, J.E.; Münch, I. Nanoscale periodic domain patterns in tetragonal ferroelectrics: A phase-field study. *Phys. Rev. B* **2016**, *93*, 174120. [CrossRef]

29. Narita, F.; Kobayashi, T.; Shindo, Y. Evaluation of dielectric and piezoelectric behavior of unpoled and poled barium titanate polycrystals with oxygen vacancies using phase field method. *Int. J. Smart Nano Mater.* **2016**, *7*, 265–275. [CrossRef]

30. Su, Y.; Liu, N.; Weng, G.J. A phase field study of frequency dependence and grain-size effects in nanocrystalline ferroelectric polycrystals. *Acta Mater.* **2015**, *87*, 293–308. [CrossRef]

31. Wang, S.; Yi, M.; Xu, B.X. A phase-field model of relaxor ferroelectrics based on random field theory. *Int. J. Solids Struct.* **2016**, *83*, 142–153. [CrossRef]

32. Su, Y.; Kang, H.; Wang, Y.; Li, J.; Weng, G.J. Intrinsic versus extrinsic effects of the grain boundary on the properties of ferroelectric nanoceramics. *Phys. Rev. B* **2017**, *95*, 054121. [CrossRef]

33. Zhao, Z.P.; Zhang, X.M.; Zhang, H.J.; Tang, H.W.; Liang, Y. Numerical investigation into pressure-assisted sintering using fully coupled mechano-diffusional phase-field model. *Int. J. Solids Struct.* **2022**, *234–235*, 111253. [CrossRef]

34. Lv, Z.; Zhang, X.; Zhang, H.; Zhou, Z.; Xu, D.; Pei, Y. Phase-field simulation of magnetic double-hole nanoring and its application in random storage. *Int. J. Smart Nano Mater.* **2021**, *12*, 157–184. [CrossRef]

35. Su, Y.; Landis, C.M. Continuum thermodynamics of ferroelectric domain evolution: Theory, finite element implementation, and application to domain wall pinning. *J. Mech. Phys. Solids* **2007**, *55*, 280–305. [CrossRef]

36. Cai, W.; Fu, C.; Gao, J.; Chen, H. Effects of grain size on domain structure and ferroelectric properties of barium zirconate titanate ceramics. *J. Alloys Compd.* **2009**, *480*, 870–873. [CrossRef]

37. Schiøtz, J.; Di Tolla, F.D.; Jacobsen, K.W. Softening of nanocrystalline metals at very small grain sizes. *Nature* **1998**, *391*, 561–563. [CrossRef]

38. Fridkin, V.M. Critical size in ferroelectric nanostructures. *Phys. Usp.* **2006**, *49*, 193–202. [CrossRef]

39. Diéguez, O.; Rabe, K.M.; Vanderbilt, D. First-principles study of epitaxial strain in perovskites. *Phys. Rev. B* **2005**, *72*, 144101. [CrossRef]

40. Liu, J.M.; Yu, L.C.; Yuan, G.L.; Yang, Y.; Chan HL, W.; Liu, Z.G. Dynamic hysteresis of ferroelectric $Pb(Zr_{0.52}Ti_{0.48})O_3$ thin films. *Microelectron. Eng.* **2003**, *66*, 798–805. [CrossRef]

41. Richman, M.S.; Rulis, P.; Caruso, A.N. Ferroelectric system dynamics simulated by a second-order Landau model. *J. Appl. Phys.* **2017**, *122*, 094101. [CrossRef]

42. Hou, Y.F.; Li, W.L.; Zhang, T.D.; Wang, W.; Cao, W.P.; Liu, X.L.; Fei, W.D. Large piezoelectric response of $BiFeO_3/BaTiO_3$ polycrystalline films induced by the low-symmetry phase. *PCCP* **2015**, *17*, 11593–11597. [CrossRef] [PubMed]

43. Hossain, M.E.; Liu, S.Y.; O'Brien, S.; Li, J. Frequency-dependent ferroelectric behavior of $BaMn_3Ti_4O_{14.25}$ at room temperature. *Appl. Phys. Lett.* **2015**, *107*, 032904. [CrossRef]

44. Guo, Y.Y.; Wei, T.; He, Q.Y.; Liu, J.M. Dynamic hysteresis scaling of ferroelectric $Pb_{0.9}Ba_{0.1}(Zr_{0.52}Ti_{0.48})O_3$ thin films. *J Phys Condens Matter* **2009**, *21*, 485901. [CrossRef]

45. Jin, L.W.; Su, Y. Effect of thermomechanical coupling on the scaling behavior of low-frequency hysteresis of $PbZr_{0.52}Ti_{0.48}O_3$ ceramics. *Electron. Mater. Lett.* **2016**, *12*, 371–375. [CrossRef]

46. Liu, J.M.; Pan, B.; Yu, H.; Zhang, S.T. Dynamic hysteresis dispersion scaling of ferroelectric Nd-substituted $Bi_4Ti_3O_{12}$ thin films. *J. Phys. Condens. Matter* **2004**, *16*, 1189–1195. [CrossRef]

47. Liu, J.M.; Chan, H.L.; Choy, C.L. Scaling behavior of dynamic hysteresis in multi-domain spin systems. *Mater. Lett.* **2002**, *52*, 213–219. [CrossRef]

48. Huang, L.M.; Chen, Z.Y.; Wilson, J.D.; Banerjee, S.; Robinson, R.D.; Herman, I.P.; Laibowitz, R.; O'Brien, S. Barium titanate nanocrystals and nanocrystal thin films: Synthesis, ferroelectricity, and dielectric properties. *J. Appl. Phys.* **2006**, *100*, 034316. [CrossRef]

49. Zhu, W.; Akbar, S.A.; Asiaie, R.; Dutta, P.K. Synthesis, microstructure and electrical properties of hydrothermally prepared ferroelectric $BaTiO_3$ thin films. *J. Electroceram.* **1998**, *2*, 21–31. [CrossRef]

50. Khan, S.; Humera, N.; Niaz, S.; Riaz, S.; Atiq, S.; Naseem, S. Simultaneous normal-anomalous dielectric dispersion and room temperature ferroelectricity in CBD perovskite $BaTiO_3$ thin films. *J. Mater. Res. Technol.* **2020**, *9*, 11439–11452. [CrossRef]

51. Silva JP, B.; Kamakshi, K.; Sekhar, K.C.; Moreira, J.A.; Almeida, A.; Pereira, M.; Gomes MJ, M. Ferroelectric polarization and resistive switching characteristics of ion beam assisted sputter deposited $BaTiO_3$ thin films. *J. Phys. Chem. Solids* **2016**, *92*, 7–10. [CrossRef]